Polar Radiant Energy in the Far-InfraRed Experiment (PREFIRE) Algorithm Theoretical Basis Document (ATBD) for the 1A-RAD and 1B-RAD data products

Brian J. Drouin, Aronne Merrelli, Timothy I. Michaels,
Erin Hokanson Wagner

Initial release, January 2025

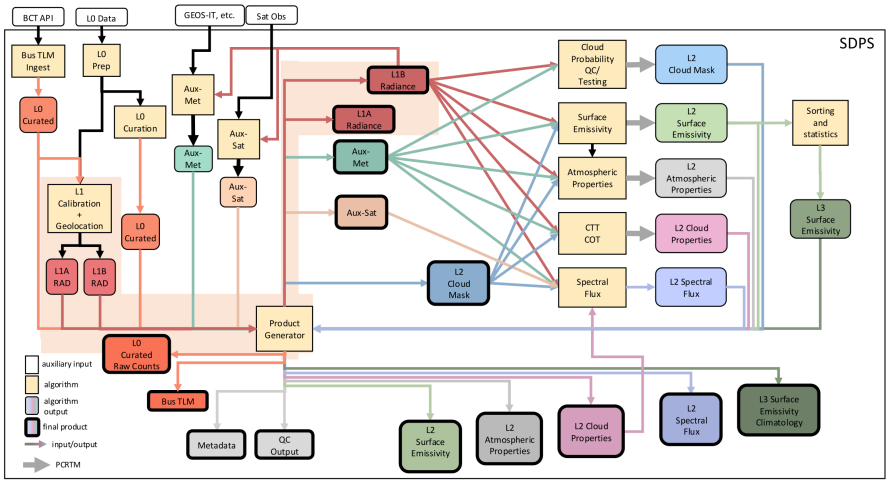

Figure 0.1: PREFIRE algorithm connectivity and flow.

Contents

1 Level-1 Radiances and Geolocation

1.1 Introduction

In this section we describe the theoretical radiometric, spatial and spectral characteristics of a space-based scanning Thermal InfraRed Spectrometer (TIRS) implemented for the NASA Polar Radiant Energy in the Far-InfraRed Experiment (PREFIRE) mission. Fundamentally, TIRS is a grating spectrometer with a slit projection on the ground aligned cross-track to the satellite motion — a so-called "pushbroom" configuration. TIRS contains a two-dimensional focal plane array detector with one dimension aligned cross-track, parallel to the slit (spatial), and the other dimension containing the spectral information from the scene, perpendicular to the slit.

The material presented here also describes the theoretical bases of the geolocation and radiometric calibration algorithms that are implemented as part of the PREFIRE Science Data Processing System (SDPS). The TIRS geometric, spectral and radiometric characteristics are described in sections 1.2 - 1.4. These are followed by sections describing the key elements of the algorithms that produce the Level-1 (L1) data products, 1A-RAD (1.5) and 1B-RAD (1.6).

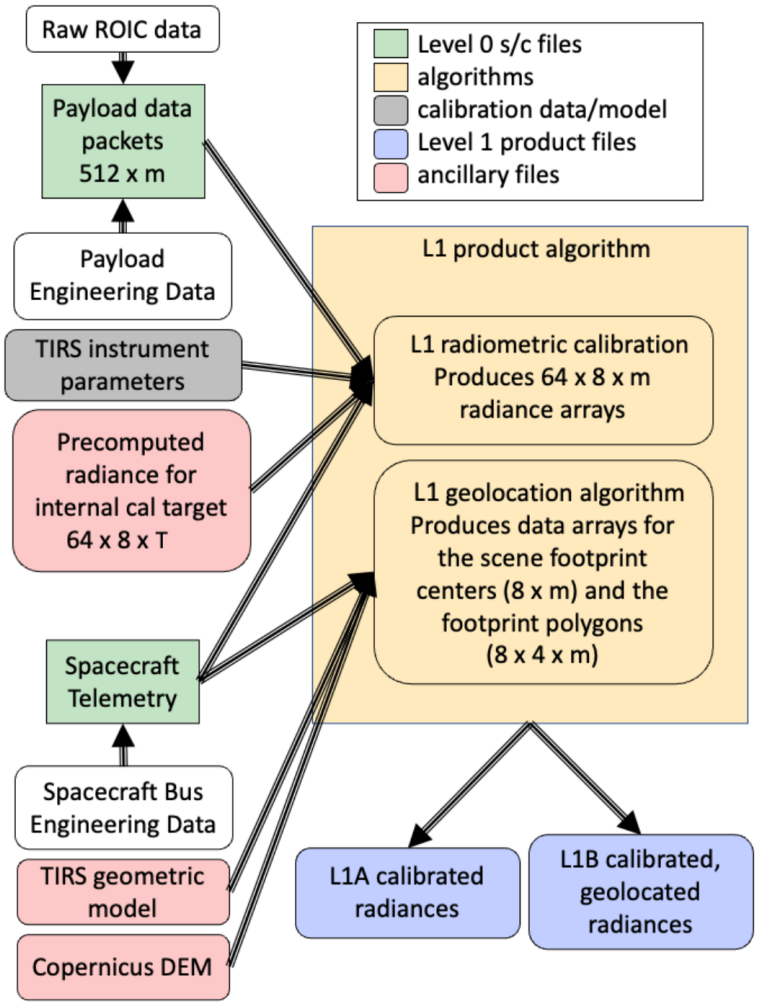

Figure 1.1: Flowchart depicting the input and output data files involved in producing Level-1 (L1) data products. The focal plane array dimensions are given, with the number of along-track frames (m), number of pre-computed calibration target temperatures (T), and the 4 vertices of the representative footprint polygons indicated.

1.2 TIRS geometric imaging considerations

The basic angular resolution parameters are controlled by the instrument focal lengths, the detector size and spectrometer slit width. In the spatial (cross-track) dimension, the angular width of the observed scene (α_{sc}) is limited by the detector size l_{d}; in the along-track (cross-slit) dimension, the angular width (α_{n}) is controlled by the spectrometer slit width l_{sw}. The focal lengths (f_{sc}, f_{n}) are different in these two perpendicular axes. The idealized angular Instantaneous Field Of View (IFOV) is then given by:

$$\alpha_{\mathrm{sc}} = l_{\mathrm{d}}/f_{\mathrm{sc}} \tag{1.1}$$

and

$$\alpha_{\mathrm{n}} = l_{\mathrm{sw}}/f_{\mathrm{n}} \tag{1.2}$$

The size of the instantaneous ground footprint for the scene, l_{sc}, is then determined by the current orbital altitude H:

$$l_{\mathrm{sc}} = \alpha_{\mathrm{sc}} H \tag{1.3}$$

The total number of cross-track scenes with cross-track dimension l_{sc} is determined by the number of detector strips (rows) in the focal plane array. Due to gaps between detector strips, the spatial sampling is not contiguous, with separations between samples in the cross-track direction equal to

$$\Delta l_{\mathrm{gap}} = l'_{\mathrm{d}} H/f_{\mathrm{sc}} \tag{1.4}$$

The total angular field of view of the swath projects to the ground swath width (l_{gs}), which is determined by the pixel width and spacing (l'_{d}) of these rows, and the number of detector rows, $M_{\mathrm{FPA}} = 8$:

$$l_{\mathrm{gs}} = M_{\mathrm{FPA}} l_{\mathrm{sc}} + (M_{\mathrm{FPA}} - 1)\Delta l_{\mathrm{gap}} \tag{1.5}$$

The detector gaps, l'_{d} are slightly more than a factor of two larger than the detector size l_{d}.

1.3 TIRS spectral sampling and resolution

The spectral sampling interval depends on the desired spectral range and number of detectors per column in the focal plane. The total number of detectors allowed in the spectral direction is n (equal to 64), including the non-spectral detection channel known as the 'zero' channel.

The ideal spectral sampling interval ($\Delta\lambda_{\mathrm{s}}$) is then the spectral range (or bandwidth), BW, divided by the number of spectral elements

$$\Delta\lambda_{\mathrm{s}} = \frac{\mathrm{BW}}{n-1} = \frac{\lambda_2 - \lambda_1}{n-1} \tag{1.6}$$

where

λ_2 = Maximum wavelength desired
λ_1 = Minimum wavelength desired

The spectral dispersion is a property of the grating related to the groove spacing l_{g}. The angular response of a grating as a function of wavelength is governed by the grating equation

$$l_{\mathrm{g}}(\sin\zeta_i - \sin\zeta_m) = m\lambda \tag{1.7}$$

where ζ_i is the incidence angle, m is the diffraction order and ζ_m is the angle at which the light of wavelength λ exits the grating for its m^{th} order, such that

$$\zeta_m = \left(\frac{m\lambda}{l_{\mathrm{g}}} - \sin\zeta_i\right) \tag{1.8}$$

Since m can be any integer, positive, negative and zero, the grating distributes light in multiple directions with overlapping effect. In an Offner spectrometer, the toroidal curvature of the grating (with X-periodicity) and compensating toroidal optic project the outgoing central dispersive rays within the f-cone at a normal incidence angle at the detector. Thus, the spectral dimension, x, of the focal plane can be described without angular factors. The intersections of the n^{th} wavelength with the focal plane may be described linearly with an effective dispersion ($l_{\mathrm{g}} = l(n-1)/\mathrm{BW}$). For spectrometry, the $M_{\mathrm{FPA}} \times n$ thermopile detector array in TIRS is situated behind an Offner spectrometer with a slit width that is chosen to be 2 pixel widths ($l_{\mathrm{sw}} = 2l_{\mathrm{d}}$) in the spectral dimension. Thus the angular response of the system in the spectral direction is linearized onto the x coordinate for convolution of the slit, the diffraction pattern, and the extent of the detector. The intersections of the n^{th} wavelength with the focal plane may be described by

$$x_n = m\frac{\lambda_n}{l_{\mathrm{g}}} + x_0 + x' \tag{1.9}$$

where x_0 is the intersection of the 0^{th} order (non-diffracted or reflected) ray in the chosen focal plane coordinate system and x' is the (nominally zero) offset of the slit center from the optical axis.

The linearized response of the system in the spectral direction for channel n ($\Re_{n,\lambda}$) is

$$\Re_{n,\lambda} = \Re_{\mathrm{slit}}(x' \pm l_{\mathrm{sw}}/2) \otimes \Re_{\mathrm{det}}(x_0 + l[n \pm 1/2]) \otimes \Re_{\mathrm{diff}}(x,\lambda) \tag{1.10}$$

where

$\Re_{\mathrm{slit}}$ = Rectangular response function representing the slit

$\Re_{\mathrm{det}}$ = Rectangular response function representing the detector

$\Re_{\mathrm{diff}}(x,\lambda)$ = Line spread function response of the optics including diffraction

λ = Wavelength

In many optical models, $\Re_{\mathrm{diff}}$ is assumed to have a small wavelength dependence and the spectral response function is fitted to a Gaussian, with another Gaussian representing the spatial spreading. However, the large spectral bandwidth of TIRS makes such an assumption circumspect, so the wavelength dependence of the instrument function is explicitly calculated at several sub-pixel (wavelength)

steps, and then convoluted with both the detector and slit sizes. The diffraction pattern is assumed to be a ideal scaled sinc function:

$$\Re_{\text{diff}}(x) = \left(\frac{\gamma \sin(\pi x/\gamma)}{\pi x}\right)^2 \tag{1.11}$$

where γ is an *a priori* weighting parameter.

The spectral resolution of the n^{th} detector element, $\Delta\lambda_n$, is the FWHM of the spectral response function, thus

$$\Delta\lambda_n = \text{FWHM}(\Re_{n,\lambda}) \tag{1.12}$$

Although diffraction spreads out the longer wavelengths at the focal plane, often into adjoining pixels, this is considered a blurring of the scenes and not a loss of signal. The convolution with the slit and detector widths properly accounts for this effect as long as the adjacent scenes are spectrally similar. Issues with geometric calibrations will be encountered in non-flat-field images.

A similar blurring, or vignetting, effect occurs in the spatial or y dimension of the sensor with

$$\Re_{sc,\lambda} = \Re_{\text{slit}}(y' \pm l_{\text{sl}}/2) \otimes \Re_{\text{det}}(y_0 + l_{\text{p}}[sc \pm 1/2]) \otimes \Re_{\text{diff}}(y, \lambda) \tag{1.13}$$

where

$\Re_{sc,\lambda}$ = diffraction limited response of the system in the spatial direction
$\Re_{\text{diff}}(y, \lambda)$ = Line spread function response of the optics including diffraction
l_{sl} = Slit length
sc = spatial scene counter from $1 \cdots 8$

1.4 TIRS radiometric model

1.4.1 Signal calculation

The thermopile detectors used by TIRS are sensitive to the total net radiation at the detector surface, from all wavelengths and incidence angles. The net radiation is a balance of thermal radiation emitted by the detector, emitted by the instrument optical elements along the optical path, emitted by the instrument internal structure, and the incident radiation from the observed scene, all expressed as at-detector irradiances (radiation incident on the detector) or exitance (radiation emitted by the detector) in units of W m^{-2}. The TIRS scan mirror can select between an Earth view, space view, or internal calibration target for the observed scene. The total net radiation can be described by a simplified model of the instrument that splits the total irradiance at the detector for channel n ($E_{\text{total},n}$) into multiple terms:

$$E_{\text{total},n} = E_{sc,n} + E_{\text{filt}} + E_{\text{inst}} - \sigma_B T_{\text{det}}^4 \tag{1.14}$$

where

$E_{sc,n}$ = Irradiance from the observed scene for spectral channel n

E_{filt} = Irradiance emitted from the order-sorting spectral filter

E_{inst} = Irradiance emitted from other optical or instrument surfaces that passes through the order-sorting filter

$\sigma_B T_{\text{det}}^4$ = Exitance emitted from the detector itself

Note that the detector is assumed to be a blackbody (unit emissivity) such that the total exitance is given by the Stefan-Boltzmann law. All but the final term are spectrally dependent (*e.g.*, the order-sorting filters' spectral transmission and emissivity).

The spectral irradiance from the scene ($E_{sc,n}$) is the spectral integral of the product of the spectral response function and the scene spectral radiance $L_{sc}(\lambda)$ and the angular integral over the incident light cone at the detector with $\cos\theta$ weighting. The spectral response function can be written as the product of the line spread function described above ($\Re_{n,\lambda_i}$), the order-sorting filter transmission ($\tau_{\text{f},\lambda_i}$) and the grating efficiency ($^1\rho_{g,\lambda_i}$):

$$\text{SRF}_n(\lambda_i) = {}^1\rho_{\text{g},\lambda_i}\ \tau_{\text{f},\lambda_i}\ \Re_{n,\lambda_i} \tag{1.15}$$

$$E_{sc,n} = \int_{\lambda_0}^{\lambda_1} \int_{\Omega} \text{SRF}_n(\lambda) L_{sc}(\lambda) \cos\theta\ d\lambda\ \sin\theta\ d\theta\ d\phi \tag{1.16}$$

Note that the light cone (Ω) in the TIRS optical path is not circular, due to the different focal lengths in the along-slit and cross-slit dimensions. The elliptical shape means the integration limits do not have simple analytic expressions. In practice, the average between the two cone angles can be used with relatively small error (less than 10%), since the focal lengths are not too different.

The non-dispersive light from the scene is detected in the broad-band 'zero' channel and corresponds to signal $E_{\text{sc},0}$, which has no order-sorting filter in the optical path. In this case, the total irradiance can be written as

$$E_{\text{total},0} = E_{sc,0} + E_{\text{inst},0} - \sigma_B T_{det}^4 \tag{1.17}$$

where the irradiance due to other optical or instrument surfaces ($E_{\text{inst},0}$) is different than the similar term in equation 1.14, due to the lack of an order-sorting filter contributing to thermal emission and reflection in the path. The scene irradiance depends on the reflective efficiency of the grating ${}^0\rho_{g,\lambda}$ and the transmission of the diamond focusing window, τ_C:

$$E_{sc,0} = \int_{\lambda_0}^{\lambda_1} \int_{\Omega} {}^0\rho_{\text{g},\lambda}\ \tau_C\ L_{sc}(\lambda) \cos\theta\ d\lambda\ \sin\theta\ d\theta\ d\phi \tag{1.18}$$

Although the instrument is designed to maximize the thermal signal from the objective, thermopile detectors are sensitive to all wavelengths incident upon the devices from the entire hemisphere above, such that $E_{sc,n}$ is only a fraction of the temperature change sensed by the detector element. In a perfect thermopile design, the internal instrument 'scene' (*e.g.*, focal plane enclosure walls) is *exactly* the same temperature as the detector, such that the device is only sensitive to the scene at the objective. Due to the heat dissipated from the

electronics, the TIRS detectors (with temperature T_{det}) are relatively warm in comparison to other instrument elements, such as the filters and optics (with temperatures T_{filt} and T_{optics}) that are typically 1 K and 4 K cooler, respectively. The L1 on-orbit radiometric calibration algorithm is designed to account for these temperature gradients as part of the time-varying offset term (see section 1.5).

The signal levels above are expressed in terms of irradiances, as that is the fundamental radiative quantity at the detector level. The radiation of the observed scene is more naturally expressed in terms of the spectral radiance, with units of W m^{-2} sr^{-1} μm^{-1}. We can compute the expected scene spectral radiance for channel n ($L_{sc,n}$) by applying the SRF in the standard way

$$L_{sc,n} = \frac{\int_{\lambda_1}^{\lambda_2} L_{sc}(\lambda)\ \text{SRF}_n(\lambda)\ d\lambda}{\int_{\lambda_1}^{\lambda_2} \text{SRF}_n(\lambda)\ d\lambda} \tag{1.19}$$

where $L_{sc}(\lambda)$ has units of W m^{-2} sr^{-1} μm^{-1}.

Our definition of SRF 1.15 does not include a normalization, which means the amplitude of the SRF includes information about the total system throughput. The SRF amplitude, defined this way, could include potential systematic biases or uncertainties (for example, we do not include the reflectivity of the mirror). However, since our fundamental radiance product is a spectral radiance, through the standard application of the SRF (1.19) the overall amplitude is automatically normalized and only the SRF spectral shape impacts the result.

Finally, each thermopile detector has a characteristic voltage related to the net at-detector irradiance described above, such that the detector responsivity ($\wp_{sc,n}$, with units V W^{-1}) and detector area (l_d^2) allow calculation of the sensible voltage

$$V_{sc,n} = l_d^2 \wp_{sc,n} E_{\text{total},n} \tag{1.20}$$

1.4.2 Instrument noise

The detector noise of the thermopile detectors is generally spectrally flat. All detector elements will have approximately the same Noise Equivalent Power (NEP), typically expressed by a constant detectivity D^*. Additional terms, such as electronics noise from the read-out integrated circuit (ROIC), could be converted from voltage to power using the instrument responsivity, and added in quadrature to get the total instrument noise.

Ultimately we need the instrument noise defined as a NEdR (Noise Equivalent delta spectral Radiance) to match the fundamental radiometric quantity reported in the 1A-RAD and 1B-RAD data products. In principle, the NEdR can be computed based on the detector D^* and electronics noise, combined with other relative instrument parameters such as the optics f-number and detector areas. In practice, the instrument NEdR is best estimated empirically by analysis of collected sensor data. In this manner, any unknowns in the original

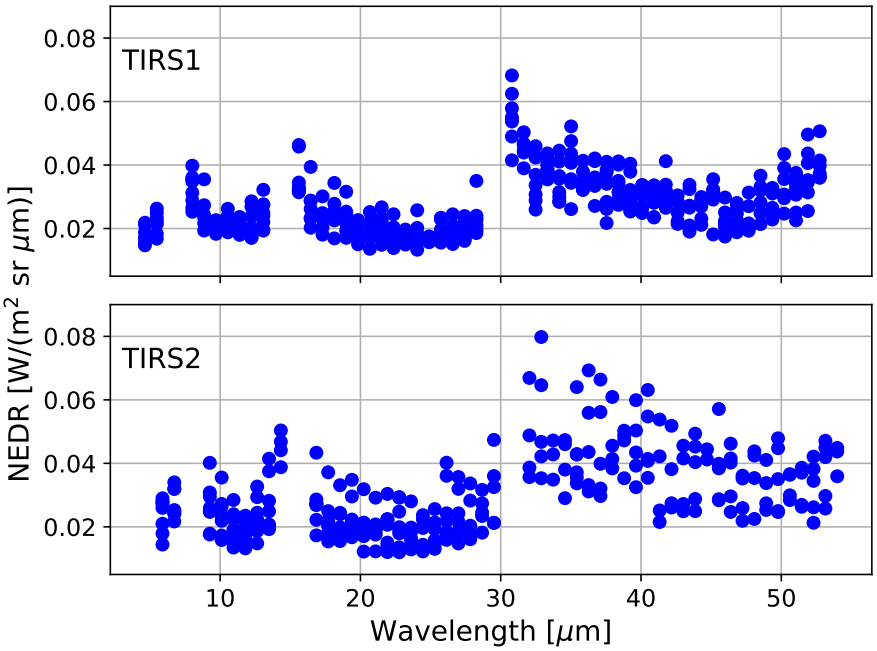

Figure 1.2: The spectral NEdR of TIRS1 and TIRS2, estimated from pre-launch radiometric calibration data. Noisy or unresponsive pixels are omitted from the plots. Values for all M_{FPA} scenes are shown, leading to multiple samples per channel on each plot — differences that are due to variability in instrument component manufacture and installation. The gaps at wavelengths $\sim$ 8, 15, and 31 μm are due to the edges of the order-sorting filters.

instrument parameters or changes in instrument characteristics during hardware integration would automatically be included in the NEdR estimate. This is particularly important for identifying bad detector elements that may change behavior over time.

Figure 1.2 shows the empirically estimated channel NEdR from the pre-launch radiometric testing of each of the two TIRS instruments. Noisy or unresponsive detector elements have been omitted from the plot. The on-orbit detector performance is often somewhat different from pre-launch estimates, and so will be replaced with on-orbit estimates if necessary.

1.4.3 Digitization

The TIRS ROICs have integrated analog-to-digital converters, and thus the associated gain, g^{IC}, has units of counts V^{-1}. An offset, o^{IC}, in the digitizer allows for all counts to be positive values. The gain and offset are specific to each ROIC, and thus equal for a series of TIRS channels. Here we assume that

all ROICs have equal gain and offset values. The signal digitization enables the TIRS data memory storage to contain arrays of integers, $\mathbb{S}$, that are $sc \times n$.

$$\mathbb{S}_{sc,n} = o^{IC} + g^{IC} V_{sc,n} \tag{1.21}$$

Raw TIRS data contain blocks of the $\mathbb{S}_{sc,n}$ arrays separated by headers to indicate housekeeping information and the target selecting mirror positions.

The factors $\tau_f, {}^n\rho_g, \Re_{sc,n}$ are determined by calibration or approximated by the system design parameters. It is common for SRFs to be normalized to unity and efficiency factors to be absorbed into $\Re$ coefficients. The choice here to have a relatively flat value of $\Re$ for each pixel derives from an engineering perspective and retains the broadband nature of these elements. For purposes of signal and noise differentiation, the signal equations will be separate for each of the 8 scenes, such that the effects of instrument and detector temperature variation will be treated as noise and assumed constant for signal.

1.4.4 Out-of-band signal

In addition to capturing the pure reflection (0^{th} order) and primary (1^{st} order) of the grating, other (higher) grating orders will propagate into the detector plane and produce signals if not absorbed or scattered by the filters. The wavelengths, at a given channel, of this undesired radiation are related through the linearized grating equation 1.9. Orders other than the 1^{st} order fall outside of the designed filter bandwidths, such that the minimal filter transmission at these positions attenuates the light.

The out-of-band term can be added by generalizing the SRF to m orders.

$$\mathrm{SRF}_{sc,n}(\lambda_i) = \sum_{m=1}^{3} {}^m\rho_{g,\lambda_i/m} \tau_{\mathrm{f},\lambda_i} \Re_{n,\lambda_i/m} \tag{1.22}$$

1.5 Level-1 radiometric calibration algorithm

During nominal operations, the instrument performs active calibration sequences in which it is commanded to first observe an external view of cold space at temperature T_{sp} for some (relatively short) length of time, then similarly observe an internal calibration target at T_{cal}. These calibration views are used in a two-point (linear) calibration equation to convert the raw counts ($\mathbb{S}_{sc,n}$) into calibrated spectral radiance ($L_{sc,n}$).

At TIRS wavelengths, cold space at $T_{\mathrm{sp}} \sim 2.7$ K produces essentially zero radiance, so the $E_{sc,n}$ term in 1.14 would also be zero. Therefore, the space view quantifies the aggregate contributions of the background signals (E_{filt}, E_{inst}, and $\sigma_B T_{\mathrm{det}}^4$ in 1.14), while the calibration target view includes the same terms as well as a scene radiance equal to blackbody emission at T_{cal}. The TIRS optical path and internal calibration are designed to be as isothermal as possible, which reduces calibration bias due to uncertainty in the blackbody target emissivity.

Therefore, the radiance from the internal calibration target is assumed to be that of a blackbody ($\varepsilon = 1$).

Combining equations 1.14 and 1.21 and taking the difference between counts measured from a calibration target view ($\mathbb{S}^{\text{cal}}_{sc,n}$) and a space view ($\mathbb{S}^{\text{sp}}_{sc,n}$), yields:

$$\mathbb{S}^{\text{cal}}_{sc,n} - \mathbb{S}^{\text{sp}}_{sc,n} = g^{IC} l_d^2 \wp_{sc,n} E_{sc,n} \tag{1.23}$$

Since the at-detector scene irradiance $E_{sc,n}$ is proportional to the at-aperture scene spectral radiance $L_{sc,n}$ we can rewrite this equation in terms of L, and lump all constants together into a single radiometric gain $g^{\text{rad}}_{sc,n}$:

$$\mathbb{S}^{\text{cal}}_{sc,n} - \mathbb{S}^{\text{sp}}_{sc,n} = g^{\text{rad}}_{sc,n} L_{sc,n} \tag{1.24}$$

For the view of the calibration target, the $L_{sc,n}$ are assumed to be blackbody radiances after applying the SRFs using equation 1.19. For efficiency, these values are pre-computed in a lookup table over a range of T_{cal}, and then linearly interpolated to the T_{cal} sampled at the time of the calibration target view. Given the interpolated pre-computed blackbody radiances $B_{sc,n,T_{\text{cal}}}$, the radiometric gain is computed as:

$$g^{\text{rad}}_{sc,n} = \frac{\mathbb{S}^{\text{cal}}_{sc,n} - \mathbb{S}^{\text{sp}}_{sc,n}}{B_{sc,n,T_{\text{cal}}}} \tag{1.25}$$

Application of the gain to the measured Earth signal allows calculation of the calibrated Earth spectral radiances, $L_{sc,n}$, designated as the 1A-RAD (Level-1a) science data product. This calculation uses the space view counts as the offset term ($\mathbb{S}^{sp}_{sc,n}$) and divides by the radiometric gain:

$$L_{sc,n} = \frac{\mathbb{S}_{sc,n} - \mathbb{S}^{\text{sp}}_{sc,n}}{g^{\text{rad}}_{sc,n}} \tag{1.26}$$

Because the background terms will drift as the instrument temperatures change, the gain and offset terms must be interpolated from the values derived at the calibration sequence times to the times for each TIRS Earth view observation. The interpolation method must replicate the temporal behavior of the background terms. More frequent calibration sequences would generally allow for simpler interpolation functions, at the cost of lost Earth-view science data. The current implementation of the radiometric calibration uses the `makima` (modified Akima piecewise cubic Hermite interpolation) function in MATLAB for the temporal interpolation. The performance of this method will be evaluated on-orbit, with the goal of maximizing the Earth-view science data that can be collected with minimal radiometric calibration error.

1.6 Level-1 geolocation algorithm

The geolocation algorithm for each TIRS Earth-view observation (consisting of $M_{FPA} = 8$ spatial scenes) has four main steps: (1) Determine the representative angular instantaneous field of view (IFOV) parameters for each scene,

accounting for instrument characteristics and spacecraft attitude. (2) Obtain the representative angular field of view (FOV) parameters for each scene, accounting for the translation of the IFOV due to spacecraft orbital motion. (3) Calculate the angular FOV intersection points with the reference Earth ellipsoid, given spacecraft geodetic coordinates. (4) Correct for the line-of-sight vector's intersection with topography. The finished results of this geolocation calculation are packaged (along with the calibrated observed radiances) in the 1B-RAD (Level-1b) science data product.

1.6.1 Scene IFOV model

Starting with the idealized angular instantaneous field of view (IFOV) described in section 1.2, the angular projections of the detector dimensions onto the Earth are determined, composed as a set of tilt (α') and azimuth (β') angles at each scene's center and four corner points. The fundamentals of how this is done are described below.

The Level-0 spacecraft (bus) data includes the spacecraft attitude (represented in quaternion form), and the satellite's orbital position and velocity vectors, all referenced to the Earth-Centered Inertial (ECI) reference frame, as well as timestamps. TIRS is bolted onto the spacecraft frame in an immovable fashion, and thus its view is directly affected by the spacecraft attitude. The nominal attitude of the spacecraft during science operations has the spacecraft's $+Y$ axis aligned with the nadir vector pointing to Earth.

The spacecraft position vector (ECI frame) and timestamp (UTC) are used to calculate the equivalent geodetic coordinates, and then to determine the spacecraft azimuth angle (β) from a finite difference of geodetic spacecraft latitude and longitude coordinate pairs (ϕ, θ) with respect to time (over a time interval of order 1 s). The calculation for β can be written as follows, in terms of spacecraft position vector components in the ECI frame (x_{ECI}, y_{ECI}), spacecraft geodetic latitude and longitude, and the orbital radius (R_b):

$$\beta = -\tan^{-1} \frac{R_b(\phi - \phi')}{\sqrt{x_{\mathrm{ECI}}^2 + y_{\mathrm{ECI}}^2}(\theta - \theta')} \tag{1.27}$$

Information from pre-flight testing of each TIRS instrument enables modeling of instantaneous field-of-view limits for each pixel, with centers $l_{sc,m}^{\mathrm{c}} = (X_{sc,0}^{\mathrm{c}}, Y_{sc,0}^{\mathrm{c}})$ defined as the projected rays normal to the focal plane from an internal detector coordinate system. The detector coordinate system places the center of all M_{FPA} 'zero' channel detectors along the $X_{sc,0}^{\mathrm{c}} = 0$ axis, with $Y_{sc,0}^{\mathrm{c}}$ values evenly spaced at

$$Y_{sc,0}^{\mathrm{c}} = (sc - 1 - (M_{\mathrm{FPA}} - 1)/2)(l_d + l_d') \tag{1.28}$$

where sc ranges from 1 to $M_{FPA} = 8$, representing each of the eight spatial scenes of each TIRS. For ideal center ray angles of each pixel, the Y-coordinates, corrected for spectral dispersion, provide the nominal tilt angle ($\alpha_{sc,n}^{c}$) which is

the angle subtending nadir and the pixel footprint. The tracing of this distortion in the spectral dimension results in a shift of the spectral response function with respect to other spectral images, so only the spatial distortion is considered in this section. These distortions $(X^{c,\pm}_{sc,n}, Y^{c,\pm}_{sc,n})$ will be measured and quantified with a geometric instrument model $(\mathcal{F})$ as offsets to the geolocated 'zero' channels, as

$$X^{c,\pm}_{sc,n} = X^{c,\pm}_{sc} + \mathcal{F}(sc, \lambda) \tag{1.29}$$

and

$$Y^{c,\pm}_{sc,n} = Y^{c,\pm}_{sc} + \mathcal{F}(sc, \lambda) \tag{1.30}$$

A line of points associated with the ground track are defined by projection from orbit using these M_{FPA} values. Spectral footprints depend on physical pixel location and dispersion corrections in the X coordinates as shown later. Additionally, the finite size of the slit and width and breadth of the pixels each must also be projected in order to track the (potentially distorted) images onto the Earth surface. Geometric calibration of the instrument provides a two-dimensional model of the pixel centroids and corners, in which any mis-alignment of the third dimension is projected onto the (actual) focal plane and blurs the 2D projection. The corner coordinates are paired as $(X^{+}_{sc,n}, Y^{+}_{sc,n})$,$(X^{+}_{sc,n}, Y^{-}_{sc,n})$,$(X^{-}_{sc,n}, Y^{+}_{sc,n})$, and $(X^{-}_{sc,n}, Y^{-}_{sc,n})$.

Adjustments to the azimuth and tilt (indicated with primes) are necessary to track the corners (and any non-ideal centroid positions), and these adjustments for α become,

$$\alpha'^{c,\pm}_{sc,n} = \frac{\alpha^{c,\pm}_{sc,n}}{|\alpha^{c,\pm}_{sc,n}|}\sqrt{(\alpha^{c,\pm}_{sc,n})^2 + (dX^{c,\pm}_{sc,n})^2} \tag{1.31}$$

where dX is the angular difference between the pixel corner x coordinate and the ideal position of the pixel centroid.

$$dX^{c,\pm}_{sc,n} = (X^{c,\pm}_{sc,n} - X^{c,0}_{sc,n})/f \tag{1.32}$$

A similar correction for β is found by

$$\beta'^{c,\pm}_{sc,n} = \tan^{-1}(dX^{c,\pm}_{sc,n}/\alpha^{c,\pm}_{sc,n}m) \tag{1.33}$$

These equations for azimuth and tilt can be easily modified to accommodate for yaw, pitch and roll with respect to the spacecraft velocity vector in which β is defined (the nadir vector has been assumed for tilt). Time-dependent spacecraft attitude information is incorporated via such modifications. For yaw correction, the value is added directly to β, and for roll the value is added to α. The pitch of the spacecraft distorts the projection in the same sense as the angular coordinate dX and can thus be added to the differential angular coordinate prior to its use in calculating α' and β'.

None of the spatial scenes directly project perpendicularly from the instrument/spacecraft to the Earth, as the rays diverge across the swath with an

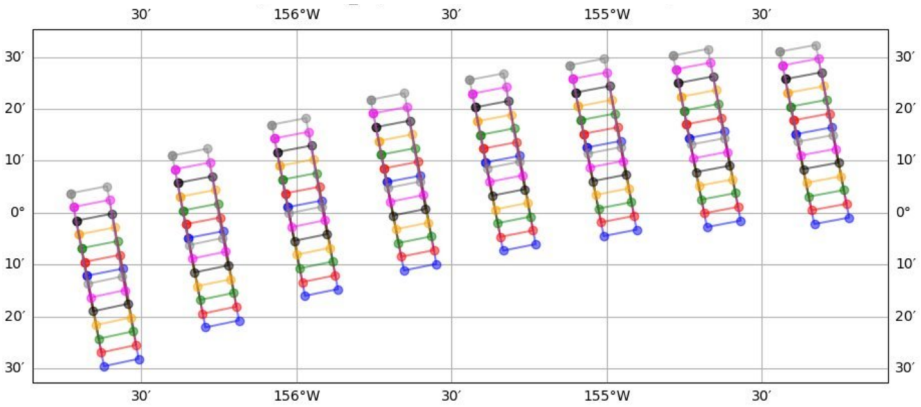

Figure 1.3: A schematic illustration of 7 consecutive along-track frames (each with M_{FPA} scenes) of geolocated PREFIRE FOVs over the equatorial Pacific Ocean (the y-axis is latitude and the x-axis is longitude). Spacecraft (along-track) motion is towards the top (from the bottom) of this view. Each frame's FOVs are outlined with a different color, with the corner vertices shown as dots. Every FOV is approximated as a quadrilateral that is longer in the along-track dimension than in the cross-track dimension. The cross-track gaps between scenes are evident, as is the substantial spatial overlap of subsequent (in time) FOVs. Note that the M_{FPA} FOVs in a single along-track frame exhibit a curvilinear 'smile' due to properties of the instrument.

observing gap in the center due to the even number of pixels. Thus the rays spread out in the cross-track direction from the instrument/spacecraft pointing direction, where the scene-specific angular dependence can be computed from the angular IFOV.

1.6.2 Scene FOV and its intersection with the Earth ellipsoid

TIRS has a finite dwell time ($t_{dw} = 0.7$ s), which is the amount of time the image is averaged (or integrated) by the detectors while the along-track dimension of the IFOV moves across the surface due to orbital motion. This corresponds to an additional along-track extent of the (non-instantaneous) FOV that is proportional to the spacecraft velocity multiplied by the dwell time. Note that half of this additional along-track extent trails the IFOV at the midpoint of the dwell time, and half leads that IFOV. Since the along-track IFOV is much larger than the orbital motion during the dwell time, successive observations will contain substantial overlap in their ground footprints. This overlap should *not* be assumed to be an integer number of frames / subsequent FOVs.

In order to to determine the full extent of each motion-smeared FOV, the IFOV calculations described in 1.6.1 are repeated three times. For the scene FOV centers, this projection is done at the midpoint of the dwell time (*i.e.*, $t_{mid} = t_{begin} + \frac{1}{2}t_{dw}$). Additional projections are done at each corner of the

scene, according to the $(X^{\pm}_{sc,n}, Y^{\pm}_{sc,n})$ described above, both at the beginning and end of the detector dwell time. The appropriate portions of these resulting IFOV coordinates are assembled into a set of FOV coordinates. To find the geodetic ground latitude, $\phi^{c,\pm}_{sc}$, and ground longitude, $\theta^{c,\pm}_{sc}$, of each point in the FOV projected onto the oblate spheroid Earth, we utilize a MATLAB routine `lookatSpheroid` which was confirmed with custom code to efficiently compute the distance to and positions on the oblate Earth. These projections to geodetic ground position assume the WGS84 ellipsoidal model.

Figure 1.3 shows a schematic example of geolocated PREFIRE FOVs over the open ocean. It illustrates the general FOV size/shape, overlap, 'smile' (due to instrument properties), and gaps between scenes. Note that since the IFOV dimensions are partly a function of orbital altitude (see 1.2), and the orbital altitude of a CubeSat in low-Earth orbit without propulsion slowly decreases with time (due to variable atmospheric drag), the detailed FOV dimensions will change over the course of the mission.

1.6.3 Corrections for topographic effects

Starting from the geodetic, ellipsoidal latitude and longitude, the earth geoid (EGM96 model) and topography are sampled in order to obtain the surface elevation at all ground points. The surface elevation is used with an iterative algorithm to update the FOV latitude and longitude positions by accounting for the line of sight vector's intersection with the elevated surface. This algorithm is implemented in a similar fashion as the VIIRS geolocation algorithm (VIIRS geolocation ATBD, 2017). The surface topography is derived from the Copernicus 90m Digital Elevation Model (GLO-90 DEM).

1.7 References

Joint Polar Satellite System (JPSS) VIIRS Geolocation Algorithm Theoretical Basis Document, Rev A, 2017. Available from `https://www.star.nesdis.noaa.gov/jpss/Docs.php`

Copernicus Digital Elevation Model (DEM), GLO-90, was accessed on 30 October 2022 from `https://registry.opendata.aws/copernicus-dem`.

2 Appendix

2.1 Table of variables and symbols

$\mathbf{A}$	averaging kernel matrix
α	angular resolution
β	azimuth angle
B	blackbody radiance
BW	spectral bandwidth
χ	convergene criterion
c	speed of light, cost function
CWP	Cloud Water Path
d	degree of freedom
ε	emissivity
ϵ	noise, error
ϕ	longitude
E	irradiance
F	flux
f	focal length
$\mathcal{F}$	function
γ	*a priori* weight
G	gravitational constant
g	gain
H	height
h	Planck's constant
I	radiance
IWC	Ice Water Content
IWP	Ice Water Path
j	counter
k	Boltzmann's constant, unknown
$\mathbf{K}$	Jacobian
λ	wavelength, Marquardt-Levenberg parameter
l	distance
L	radiance
LTS	Lower Tropospheric Stability
LWC	Liquid Water Content
LWP	Liquid Water Path
M	counter, mass
m	number of along-track frames
$\mathcal{M}$	matrix
N	counter
n	channel
$\mathcal{N}$	normal distribution
ν	frequency

NEdT	Noise-Equivalent delta Temperature
o	offset
Ω	solid angle
p	pressure
P	probability
PWV	Precipitable Water Vapor
Q	water vapor
ρ	reflection coefficient
R	radius, resistance, cost-function change
$\Re$	response function
$\wp$	responsivity
σ_B	Stefan-Boltzmann constant
$\mathbb{S}$	signal level in digitized counts
S	covariance
SI	Segmentation Index
SNR	Signal-to-Noise Ratio
SRF	Spectral Response Function
θ	latitude, potential temperature, polar coordinate angle
τ	transmission, optical depth
T	temperature
TR	Training Radiances
TREM	TRaining Eigenvector Matrices
t	time
ϕ	polar coordinate angle
V	voltage
v	velocity
x, y, z	position coordinates
z	convergence, standard deviation of scaled differences
$\mathbf{x}$	state vector
X	focal plane position
$\mathbf{y}$	measurement vector
Y	focal plane position
ζ	incidence angle

Table 2.1: Table of variables and symbols.

2.2 Abbreviations and acronyms

ADM	Angular Distribution Model
AIRS	Atmospheric Infrared Sounder
ATBD	Algorithm Theoretical Basis Document
CERES	Clouds and the Earth's Radiant Energy System
DEM	Digital Elevation Model
DOF	Degree of Freedom
ECI	Earth-Centered Inertial
ECMWF	European Centre for Medium-Range Weather Forecasts
EOF	Empirical Orthogonal Function
FIR	Far-InfraRed
FOV	Field Of View
FPA	Focal Plane Array
FWHM	Full Width at Half Maximum
IFOV	Instantaneous Field Of View
IFS	Integrated Forecasting System
LW	Longwave
MIR	Mid-InfraRed
NASA	National Aeronautics and Space Administration
NEP	Noise Equivalent Power
NEdR	Noise Equivalent delta spectral Radiance
OLR	Outgoing Longwave Radiation
PCRTM	Principal Component-based Radiative Transfer Model
PREFIRE	Polar Radiant Energy in the Far-InfraRed Experiment
ROIC	Read-Out Integrated Circuit
RMSE	Root Mean Square Error
SDPS	Science Data Processing System
SSF	Single Scanner Footprint
SRF	Spectral Response Function
TCWV	Total Column Water Vapor
TIRS	Thermal InfraRed Spectrometer
TOA	Top of Atmosphere
UTC	Coordinated Universal Time
VZA	Viewing Zenith Angle
WV	Wavelength

Table 2.2: Abbreviations and acronyms.

2.3 Figure listing with links

#	Brief Description
0.1	PREFIRE algorithm connectivity and flow
1.1	Level-1 data processing flowchart
1.2	Measured NEdR
1.3	Schematic illustration of FOVs

Table 2.3: List of Figures in this ATBD.